PAPER

A compact and cost-effective laser desorption source for molecular beam generation: comparison with simulations

To cite this article: Afik Shachar et al 2021 J. Phys. B: At. Mol. Opt. Phys. 54 175401

View the article online for updates and enhancements.

You may also like

- The very high *n* Rydberg series of Ar¹⁶⁺ in Alcator C-Mod tokamak plasmas
 J E Rice, F Sciortino, M Gu et al.
- Diffractive focusing of a uniform Bose-Einstein condensate Patrick Boegel, Matthias Meister, Jan-Niclas Siemß et al.
- Auger cascade initiated by the Coster–Kronig transition from the Kr 3p core-hole states
 Y Hikosaka, P Lablanquie, T Kaneyasu et al.



IOP ebooks™

Bringing together innovative digital publishing with leading authors from the global scientific community.

Start exploring the collection-download the first chapter of every title for free.

A compact and cost-effective laser desorption source for molecular beam generation: comparison with simulations

Afik Shachar^{1,3}, Itai Kallos^{1,3}, Mattanjah S de Vries² and Ilana Bar^{1,*}

- ¹ Department of Physics, Ben-Gurion University of the Negev, Beer-Sheva 8410501, Israel
- ² Department of Chemistry & Biochemistry, University of California Santa Barbara, CA 93106, United States of America

E-mail: ibar@bgu.ac.il

Received 5 July 2021, revised 29 August 2021 Accepted for publication 9 September 2021 Published 30 September 2021



Abstract

The development of laser-desorption jet-cooling has enabled the study of low vapor pressure molecules in the gas phase. Here, we design and assemble a unique compact laser-desorption source comprising simple parts for sample movement and desorption and attach it to a home-built time-of-flight mass spectrometer for spectroscopic studies of jet-cooled biomolecules. Modeling and visualization of the molecular beam (MB) by the direct simulation Monte Carlo method provides spatial evolution and global features of the flow and new insights into source operation. The system is validated by determining operational parameters from the simulation and comparing them with the resulting resonance-enhanced two-photon ionization (R2PI) signal of tryptamine. The signal measurements in the origin band transitions region provide an R2PI spectrum resembling that previously acquired from heated samples, indicating seven conformers in the MB. Due to the potential of this source, we expect that it will reveal its feasibility through coupling to other systems and various spectroscopies.

Keywords: laser-desorption, ionization spectroscopy, biomolecules, direct simulation Monte Carlo

(Some figures may appear in colour only in the online journal)

1. Introduction

The early days of molecular beam (MB) experiments in the 1960s have been called 'the alkali age' because of the limitation to alkali atoms imposed by hot wire detectors [1]. The introduction of universal mass spectrometer (MS) detection extended the field to what one now might call a 'volatile age', still only providing MBs of species with sufficient vapor pressure or stability upon heating. This final limitation was overcome with the introduction of laser-desorption jet-cooling (LDJC) sources [2–6]. A large range of compounds

has since been studied by the combination of this technique with a variety of laser spectroscopies [7–12], including small peptides [13], DNA bases [14, 15], and polymers with masses of several thousand AMU [16, 17]. In this approach, vaporization by a laser pulse in the high-pressure region of a pulsed supersonic expansion forms an MB of intact and cold molecules. Cooling by subsequent entrainment in the pulsed jet stabilizes the molecules by reducing the internal energy and enables high-resolution spectroscopic studies. Laser-desorption (LD) differs from matrix-assisted laser desorption ionization (MALDI) [18–24], since ionization is not part of the process. MALDI combines those two steps with a single laser providing no optical spectrum. Separate wavelength-dependent post-desorption ionization makes it possible to combine laser spectroscopy and MS in one

^{*} Author to whom any correspondence should be addressed.

³ These contributed equally.

instrument. Among other applications, this combination is key to studying structure and dynamics in *isolated* biomolecules.

The process of neutral LD is poorly understood. The general idea is that fragmentation is minimized when the time scale for heating is shortened [6, 8]. Thermal heating occurs at slow rates $(10^0-10^2~{\rm Ks}^{-1})$, and for some compounds significant vapor pressures can be obtained only at high temperatures, leading to unfeasible experimental conditions and high levels of thermal decomposition. In contrast, laser-induced heating occurs at much higher rates $(10^{10}-10^{12}~{\rm Ks}^{-1})$, corresponding to a 1000 K temperature jump in a typical 10 ns laser pulse. At these heating rates it appears that the intermolecular bonds are broken before the intramolecular bonds, promoting intact vaporization [25–29].

Up to now, a limited number of studies on MB features for various LDJC geometries has been reported [2, 4, 5, 30–33]. Also, calculations based on molecular dynamics, direct simulation Monte Carlo (DSMC), and combined MD–DSMC methods [34–41] are in use for studying different features of material removal from targets and dynamics of plume expansion in laser ablation/desorption and MALDI of organic solids. Nevertheless, understanding the dependence of MB characteristics on LD source design parameters and experimental conditions is still far from complete.

Here, we report modeling by the DSMC method [42], applied to a novel compact LDJC design, and describe, in detail, the source design and data acquisition synchronization for obtaining stable signals. This LDJC source includes simple parts for sample movement and laser beam delivery. The modeling results assist source characterization and optimization through tryptamine (TRA) ionization, including an indole moiety and a flexible ethylamino side chain. The modeling and evaluation allow visualizing the MB formation and gas flow and provide further insight. TRA plays a role as a neuromodulator or neurotransmitter and has been subject to previous studies in MBs [43-53] by applying thermal heating of its samples to temperatures >100 °C, instead of LD. The resonance-enhanced two-photon ionization (R2PI) spectrum with the new source produced similar results to those previously observed by thermal evaporation, showing features related to seven conformers.

2. Methods

2.1. Source design, technical details, and operation mode

Figure 1(a) shows the schematic of the working principle of the LD, where the transformation of intact molecules into a supersonic beam occurs. Figure 1(b) presents an expanded cross-sectional view of the desorption source with the included components and the load-lock assembly. The source consists of a 6" stainless steel cube containing all the necessary desorption and load-lock assembly mechanisms allowing fast sample bar exchange. The cube includes a sample bar, x and z linear translation assemblies, optics for desorption laser beam delivery, a supersonic jet valve, and a skimmer. Pumping this chamber with a 400 l s⁻¹ turbo molecular pump (Alcatel, ATP 400) results in typical background pressures

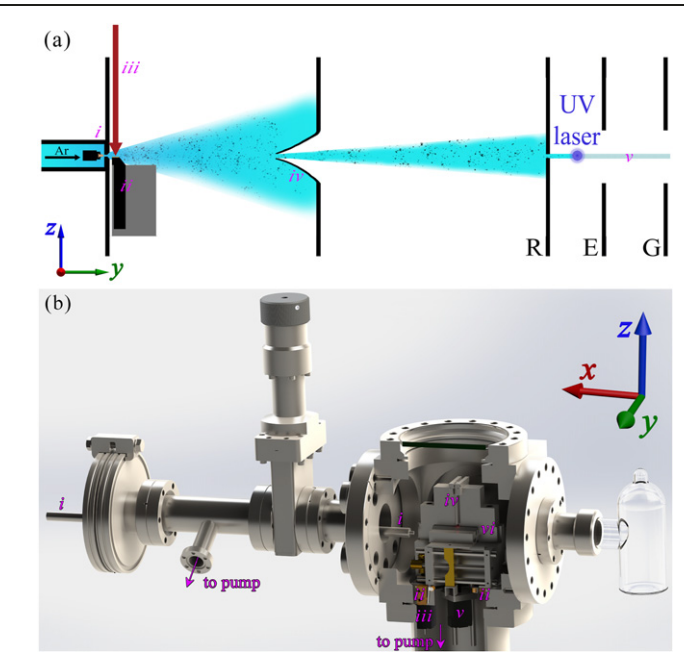


Figure 1. (a) Schematic of the working principle of LD of intact molecules and their supersonic expansion including (i) pulsed valve, (ii) sample holder with sample on its top and in front of the valve, (iii) infrared laser beam, (iv) skimmer and (v) ion source and (b) expanded desorption source (cross-sectional view) and the load-lock assembly, showing the parts: (i) guiding rod passing through the load-lock, (ii) micro-switches, (iii) x-axis stepper motor, (iv) optic fiber holder, (v) z-axis stepper motor, and (vi) sample holder.

of $\sim \! 2 \times 10^{-7}$ Torr. The carrier gas (Ar) is introduced into the chamber by a pulsed valve (Parker Hannifin, Series-9) with a 0.79 mm diameter cone-shaped orifice and polyether ether ketone poppet. This shape was selected since, as previously established [54], it produces better-collimated MBs with higher densities and improved translational cooling. A stream of Ar at a backing pressure of $\sim \! 10$ bar passes through the pulsed valve, operated at 10 Hz, cooling the entrained desorbed molecules.

The valve is magnetically activated, with current pulsed through a solenoid generating a magnetic field that pulls back a plunger and opens the orifice. We selected this valve to be compatible with LD source compactness and vacuum chamber pumping capabilities, considering its robustness, commercial availability, relatively low cost, and its widespread use in the field of atomic and MBs. Other pulsed valves are in use for producing supersonic beams, including the piezo-actuated valve [55], 'Jordan' valve [56], Nijmegen pulsed valve [57], and the Even-Lavie valve [58]. These valves operate by different opening mechanisms [59] and produce MB pulses of different durations, intensities, speed distributions, and temporal profiles.

The sample holder ((vi) in figure 1(b)) includes two parts, the bottom one machined out of stainless steel (47 × 16.5 mm) with an isosceles trapezoid groove underneath, securing the holder in place, and the top sample bar made of solid graphite, with a right trapezoid shape to reduce gas flow obstruction. The latter includes a channel (2 mm width and 0.1 mm deep) running along its top, allowing sample material deposition. The

use of a graphite sample bar yields improved experimental results attributed to its high heat capacity [60].

We prepare samples by mixing solid TRA (Sigma-Aldrich, 98% purity), without further purification, with graphite powder (Sigma-Aldrich, 282 863) at a 4:1 weight ratio. This mixture is ground by a mortar and pestle to a fine powder and then firmly pressed into the channel. The sample is positioned ~ 1 mm in front of the valve, and new material is introduced continually via x-axis linear translation by a stepper motor (Applied Motion, HT08-221), (iii) in figure 1(b). A mechanism of worm gears and threaded rods converts the rotation to horizontal motion with minimal friction using ball bearings, appropriate metals, and grease. The high torque stepper motor can achieve sample replenishment at speeds of up to 0.3 mm s⁻¹ with typical scanning speeds of $0.01-0.02 \text{ mm s}^{-1}$, scan times of up to 3 h per pass, for single or multiple passes along the sample. The sample movement is accurate down to a few μm per desorption pulse at 10 Hz repetition rate, assuring steady and consistent introduction of newly desorbed molecules into the MB.

Samples can be quickly replaced (\sim 5 min turnaround) by the load-lock system, consisting of a gate valve, a 2-3/4" diameter tube, a rod guiding the sample, a customized ConFlat flange, and a rotary vane pump (Alcatel, Pascal 2005C) for chamber evacuation. An Arduino controlled stepper motor linear actuator (PrimoPal, PHL20N30-4S05-AA4IN) positioned under the sample assembly (v) in figure 1(b) [sets the zaxis position (height) of the sample. The stepper motor body and the linear actuator are attached to the stationary rear and movable front parts of the transitional assembly, respectively, allowing the raising and lowering of its front half (including the sample holder) at 3.175 μ m/step via motor rotation. Shorter intervals ($\sim 1 \mu m$) are possible with microstepping, but these small steps do not significantly affect the ionization signal intensity, and therefore 15 μ m height increments are used. Since the linear actuator requires rotational movement for vertical motion, it provides the advantage that sliding does not occur due to vibrations (and gravity). Hence, the sample height relative to the valve orifice remains fixed almost indefinitely. Both stepper motors are positioned inside the vacuum chamber, connected to stepper motor drivers (Applied Motion, STR2), controlled by an Arduino uno microcontroller scripted in-house, and operated directly/remotely via a universal serial bus and a LabVIEW program. Upon measurement completion, the linear translation of the sample stops automatically, and a home-built remote shutter blocks the LD beam to avoid sample waste. The remote shutter consists of an Arduino nano microcontroller, mini servo motor, and 3D printed parts, allowing communication with the LabVIEW program via NI-DAQmx.

Sample molecules are desorbed using the fundamental of a Q-switched neodymium-doped yttrium aluminum garnet (Nd:YAG) laser (Continuum, Surelite I, 1064 nm, 10 Hz, ~5 ns pulses), (*iii*) in figure 1(a). This wavelength is selected since it leads to low fragmentation of molecular analytes and is in extensive use in previous LD studies [13–15, 31–33]. Generally, the desorbing laser wavelength should match the absorption characteristics of the substrate/matrix while preventing

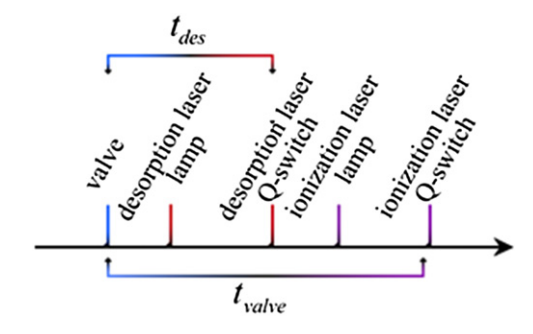


Figure 2. Timing scheme for laser-desorption and resonance enhanced two-photon ionization, with labeled time-delays, t_{valve} relative to the ionizing laser Q-switch, and t_{des} relative to the valve opening time.

overlap with those of the adsorbate. Hence, photochemical interaction and heating of the adsorbate at this wavelength are not expected but rather substrate heating. Yet, it is worth noting that reports on LD of molecular targets by lasers of other wavelengths are available, including, for instance, 248 nm from a KrF excimer laser [5, 17, 19, 20], 532 nm from a frequency-doubled Nd:YAG laser [18, 19, 30], and 10.6 μ m from a CO₂ laser [2, 19].

The Nd:YAG beam is coupled into a 550 μ m core, multimode optical fiber (Thorlabs, MHP550L02), positioned between the laser beam and the vacuum chamber. Then this optical fiber is coupled into a 600 μ m core vacuum compatible patch cable (Thorlabs, MV63L1) through a 600 μ m core feedthrough (VACOM, MM600IR-FSMA1) mounted on the side of the desorption chamber. The fiber (numerical apertures of 0.22) is attached through subMiniature version A connectors. The end of the optical fiber, positioned inside the vacuum chamber, is cleaved, and held firmly in place by a stainlesssteel cylinder, in front of the valve orifice, at a \sim 1 mm distance ((iv) in figure 1(b)). The desorption beam spot-size is controlled by altering the optical fiber height above the sample. The laser fluence is adjusted by two linear polarizers and a half-wave plate before beam coupling into the optical fiber, leading to a laser beam of ~ 1 mm diameter and ~ 0.4 J cm⁻² fluence for TRA desorption. Following desorption, the vapor entrains in the supersonic expanding carrier gas (Ar, 99.995% purity) for cooling, and then the MB passes through a 2 mm diameter skimmer (Beam Dynamics Inc., type I) with the apex positioned at 68 mm distance, opposite to the valve.

Following skimming, the MB enters a differentially pumped detection chamber of a TOFMS held at a typical pressure of 7×10^{-8} Torr by an Alcatel, ATP 150 turbo molecular pump system. The detection chamber houses a standard three plate electrostatic lens assembly containing repeller (R), extractor (E), and ground (G) plates [61–63]. The TRA molecules are probed by the focused ionizing laser, midway between the R and E electrodes, and accelerated toward the detector. TRA parent and fragment ion detection is realized by a two-stage multichannel plate detector (El-Mul Technologies), amplified by a homemade trans-impedance preamplifier, and measured by a 1 GHz digital oscilloscope (LeCroy, Waverunner 6100A). Data is accumulated and stored on a PC running a LabVIEW program.

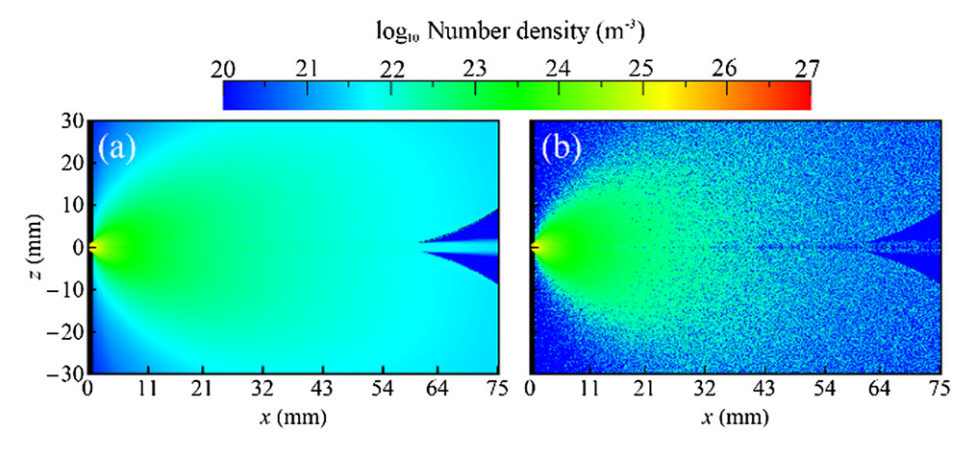


Figure 3. Simulated number density, following the admission of $\sim 2.5 \times 10^{26} \,\mathrm{m}^{-3}$ Ar atoms (backing pressure of ~ 10 bar) into a vacuum chamber at ~ 300 K through a conical orifice (left side) of 0.79 mm diameter and transmission through a 2 mm aperture skimmer (right side) while symmetrizing the 2D flow around the *x*-axis for (a) steady-state conditions and for (b) time-evolved flow at $\sim 77 \,\mu \mathrm{s}$ after gas entrance.

It is important to note that we also tested the source operation for other molecules, including the less volatile guanine, optimized the desorption efficiency, and obtained its preliminary R2PI spectrum. Since the goal was to build the source as compact as possible, we did not attempt to optimize the relative valve and skimmer positions but only the sample holder height (see below). The design and development of custom parts assure compatibility with standard assemblies for obtaining the most intense jet and highest possible signals under these experimental conditions.

2.2. Simulations by the direct simulation Monte-Carlo technique

We perform the simulations for gas flow and MB formation with the DSMC method [42]. Briefly, this numerical method treats a collection of simulated particles, representing the properties of many physical particles (typically $\sim 10^{10}$) that propagate simultaneously. It is worth noting that gas flows simulations are meaningful for the mean free path of particles of the same order or greater than the representative physical length scale (Knudsen number >1). We should recall that DSMC results suffer from two accuracy aspects, explicitly, the statistical error and the scaling factor per simulated particle [64]. The macroscopic properties of the flow field are obtained by sampling the particles within a cell, requiring an appropriate number of particles per cell to minimize the statistical error. The standard deviation of the scatter is of the order of the inverse square root of the sample size [65]. As for the scaling factor, it represents a group of real molecules having the same properties and a lower factor reduces the error. The factor selected here 10¹⁰ provides reasonable DSMC results for a two-dimensional (2D) problem [42].

The simulation volumes resemble the corresponding chambers in our experiment, consisting of a series of subcells. They allow calculating the probability of a collision between a pair of simulated particles during a time interval. We simulate the collisions using the variable hard sphere model [42]. This model employs isotropic scattering in the center-of-mass reference frame and definite diameter of the classic hard-sphere

(varying with the relative speed of the colliding pair). Then subsequent update of the positions of the simulated particles occurs while accounting for energy transfer in case of collisions and leading to the next calculation step.

We used the classical Larsen–Borgnakke approach [66] with quantum harmonic oscillator model [42], implemented in DSMC, for calculating the inelastic collisions and the vibrational energy redistribution in the desorption simulations. We approximate the TRA by a reference diameter of ~8.7 Å, viscosity-temperature power law of 0.75, and vibrational energies calculated with the Becke three-parameter hybrid functional combined with the Lee–Yang–Parr correlation functional (B3LYP) [67, 68], and the 6-311++G(d,p) basis set. The simulations were performed with the DS2V program [69] and the gas flows could be followed by considering the time steps for particle propagation.

2.3. Measurements of mass and resonance enhanced two-photon ionization spectra

We obtain the MS and mass-selected R2PI spectra of TRA by determining the mass-to-charge (m/z) via measurement of ions TOF and the gated ionization signal, respectively. The signal resulted from a tunable UV beam (\sim 5 ns pulses, 10 Hz repetition rate, \sim 1 μ J per pulse), focused by a 350 mm plano-convex lens. This beam was obtained from a frequency-doubled pulsed dye laser (Lambda Physik, FL3002) with Rhodamine 6G dye, pumped by a frequency-doubled Nd:YAG laser (Continuum, Powerlite 7010). The scanning of the laser frequency of this beam across the $S_1 \leftarrow S_0$ electronic transition results in one-color R2PI spectrum of TRA. Process synchronization is controlled by two delay generators (an inhouse built and a Stanford Research Systems, DG535) with the timing scheme shown in figure 2.

For simplicity, the Q-switch delay of the UV laser serves as the primary trigger, and the pulsed valve opening delay, t_{valve} , is set relative to it, allowing control of the on-axis probing of the MB by the ionization laser. The trigger of the Q-switch delay of the desorption laser, in relation with the valve trigger, t_{des} , controls the laser-desorbed vapor entrainment inside

the carrier gas pulse. The lamps of the two lasers are triggered before the corresponding Q-switch delays to provide optimal laser pulse energies. This scheme decouples the two degrees of freedom, cooling, and entrainment in the system, allowing simple ion signal optimization.

3. Results and discussion

3.1. Gas flow simulations

Initially, we perform a steady-state simulation resembling the operating conditions while accounting for Ar gas at 10 bar backing pressure, flowing through a cone-shaped valve, and skimmed by a 2 mm aperture skimmer (left and right side, respectively, of figure 3(a)). Then the simulation of the time-evolving MB is carried out, figure 3(b), while opening the pulsed valve for 100 μ s (to mimic the experimental conditions), keeping the other parameters unchanged, and symmetrizing the 2D flow around the x-axis. Comparison of the two simulations in figure 3 shows that for steady-state and for time-evolving MB high on-axis beam densities are produced, expressed by penetration of relatively dense Ar through the valve and a sparser density across the skimmer. The general appearance differs only in MB granularity due to a relatively lower number of simulated particles in (b), implying a large enough sample size and leading to reasonable flow representation by the non-empty cells.

Following analysis of the flow at the time it reached the skimmer (as shown in figure 3), initial conditions for the second simulation of gas flow across the skimmer and into the interaction chamber are obtained, corresponding to a \sim 560 m s⁻¹ velocity in the flow direction and a number density of \sim 7.5 \times 10²¹ m⁻³. This velocity is consistent with the calculated terminal-velocity obtained from the analytical model [70].

Figures 4(a)–(c) show snapshots of the transmitted MB, following the flow across the skimmer and into the interaction region, midway between the R and E electrodes (magenta arrow) of the TOFMS. In figure 4(a), relatively high Ar density penetrates through the skimmer and only sparser density through the R hole. This changes at longer delays, following the valve opening, showing that at 250 μ s a higher density passes through the R hole. We present the average number density in the interaction region for each time step together with the standard errors, figure 4(d), by sampling the nonempty cells. This graph shows a steep rise in the interaction region with peak density at $\sim 260 \mu s$ (accounting for ~ 40 μ s between valve opening and the gas reaching the skimmer apex) and then a steep fall \sim 60 μ s later. The gas pulse center arrives in the interaction region at \sim 290 μ s after valve opening.

These results provide insight into the gas flow along the TOFMS and can be compared to the measured time delays (see below). We obtain some understanding of the desorption process by simulating the Ar flow in absence, figure 5(a) and presence of a sample bar positioned at different heights (0.6, 1.0, and 1.5 mm) under the valve orifice center, figures 5(b)–(d). The sample bar insertion interrupts the

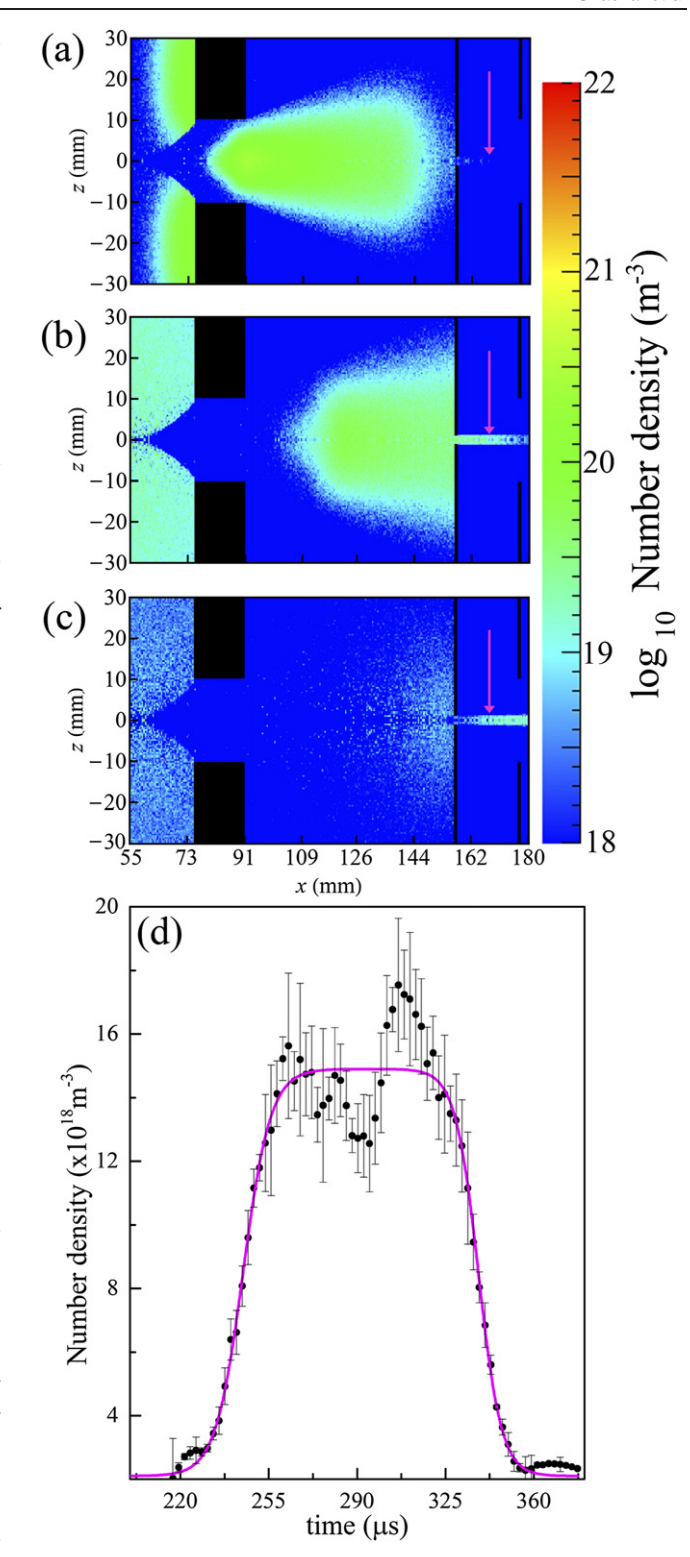


Figure 4. Snapshots of the simulated number density of Ar admitted through the skimmer at number density of $\sim 7.5 \times 10^{21} \ {\rm m}^{-3}$ moving at $\sim 560 \ {\rm m \ s}^{-1}$ in the flow direction for (a) ~ 197 , (b) ~ 249 , and (c) $\sim 334 \ \mu {\rm s}$ after valve opening, and (d) a plot of the temporal evolution of the number density in the interaction region, including standard error bars. The magenta arrows indicate the interaction region (midway between the R and E plates of the time-of-flight MS).

steady-state Ar flow by partially blocking and deflecting the MB upward. The extent of deflection changes as a function of

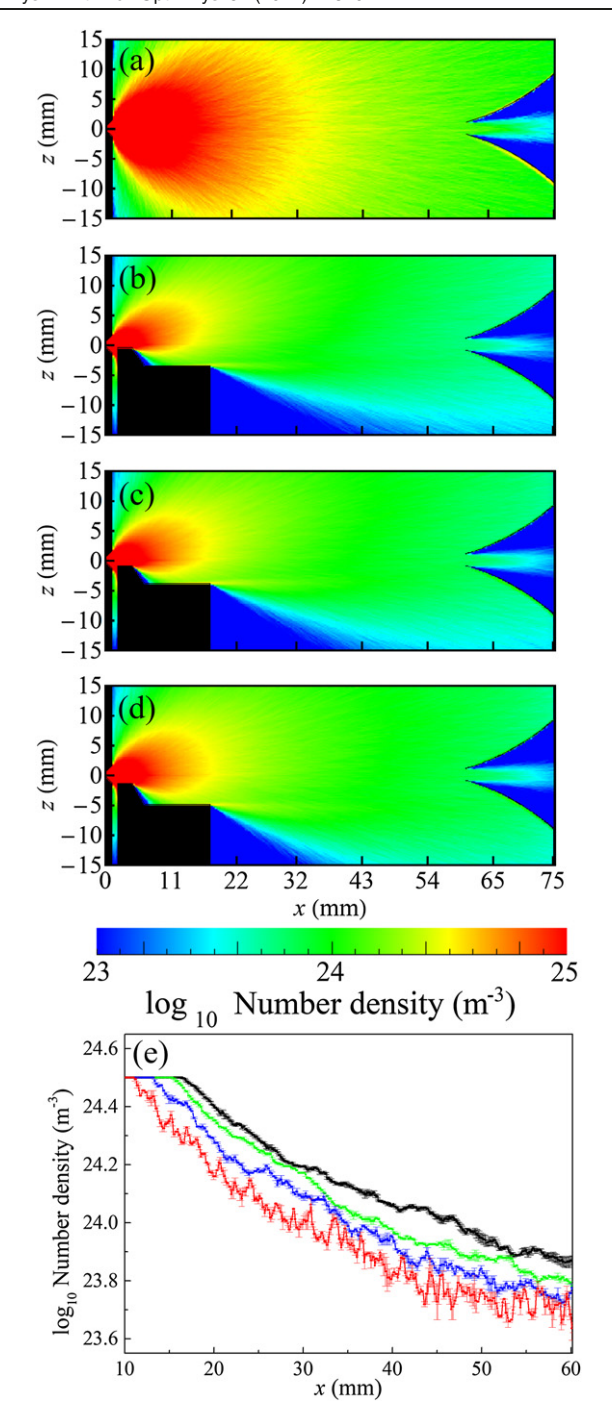


Figure 5. Steady-state simulation of Ar number density, following the admission of the MB into the source chamber through a conical orifice of 0.79 mm diameter, (a) in absence and presence of a sample bar at (b) 0.6, (c) 1.0, and (d) 1.5 mm below the valve orifice center, and (e), a plot comparing the number density for flow in absence of the sample bar (black) and in its presence at 0.6 (red), 1.0 (blue) and 1.5 mm (green).

the sample bar height and is more pronounced in figure 5(b). The blocking and deflection of the MB are even more prominent in figure 5(e), which shows the on-axis number density of Ar as a function of the distance from the valve orifice in the absence and presence of the sample bar at the three heights. This figure clearly shows somewhat lower number

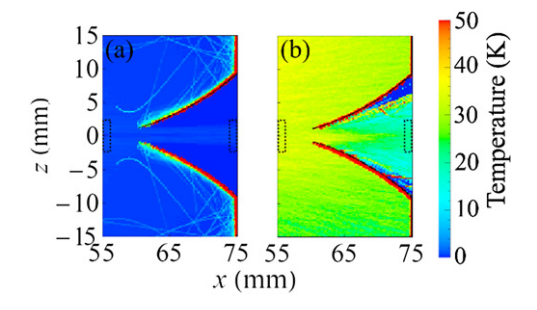


Figure 6. Comparison of the translational temperatures of Ar before entering the skimmer, with the sample bar (a) absent and (b) present (0.6 mm below the valve orifice center). Translational temperatures, before and following the skimmer, are calculated from the left- and right-black dashed rectangle region values.

density upon sample bar insertion, being more pronounced for the higher sample bar positions across the MB expansion (up to the skimmer apex). Support for these findings comes from the experimental results of reference [5] and our experimental results (see below).

Furthermore, the results obtained by the simulations allow comparing the translational temperatures of Ar before entering the skimmer, figure 6, in the absence (a) and presence (0.6 mm below the valve orifice center) (b) of the sample bar, which is the geometry used for LD of TRA. Averaging the translational temperatures within the left black dashed rectangles leads to $\sim\!\!3$ and $\sim\!\!35$ K, respectively, manifesting an increase upon sample bar interference. We attribute this increase in translational temperature to the collisional energy transfer from the entraining TRA molecules to Ar. Yet, following Ar passage through the skimmer, it is further cooled to translational temperatures of 2 and 17 K (averaged values within the right black dashed rectangles) in absence, figure 6(a), and presence, figure 6(b), of LD, respectively.

Finally, we simulate the TRA desorption by introducing a surface of 1 mm length at 0.6 mm below the valve orifice, figure 7(a). The ejection of hot TRA molecules from the surface starts 10 μ s before valve opening and lasts for 50 μ s. Three times repetition of the time-evolving simulations led to the representative snapshots of one simulation, which present the flow from the pulsed valve (0 mm) to the skimmer base (75 mm) at different times from valve opening (\sim 13, \sim 42, and \sim 65 μ s), figures 7(a)–(c). These snapshots clearly show lower number density at the MB front, where the introduction of warmer, desorbed TRA molecules occurs. Support for this observation comes from the corresponding snapshots of the MB temperature, shown in figures 7(d)-(f), where regions of warmer Ar are visible for the respective spots of lower number density. This observation indicates heat transfer from the hot desorbed TRA to the colder Ar, leading to a cooling of the entrained TRA molecules.

Averaging on-axis number density values of each of the three simulations results in the blue curve of figure 8. Comparing this curve to that obtained without desorption (red curve), a dramatic drop in Ar number density occurs at the MB front upon desorption, accompanied by TRA cooling, as shown in figure 7.

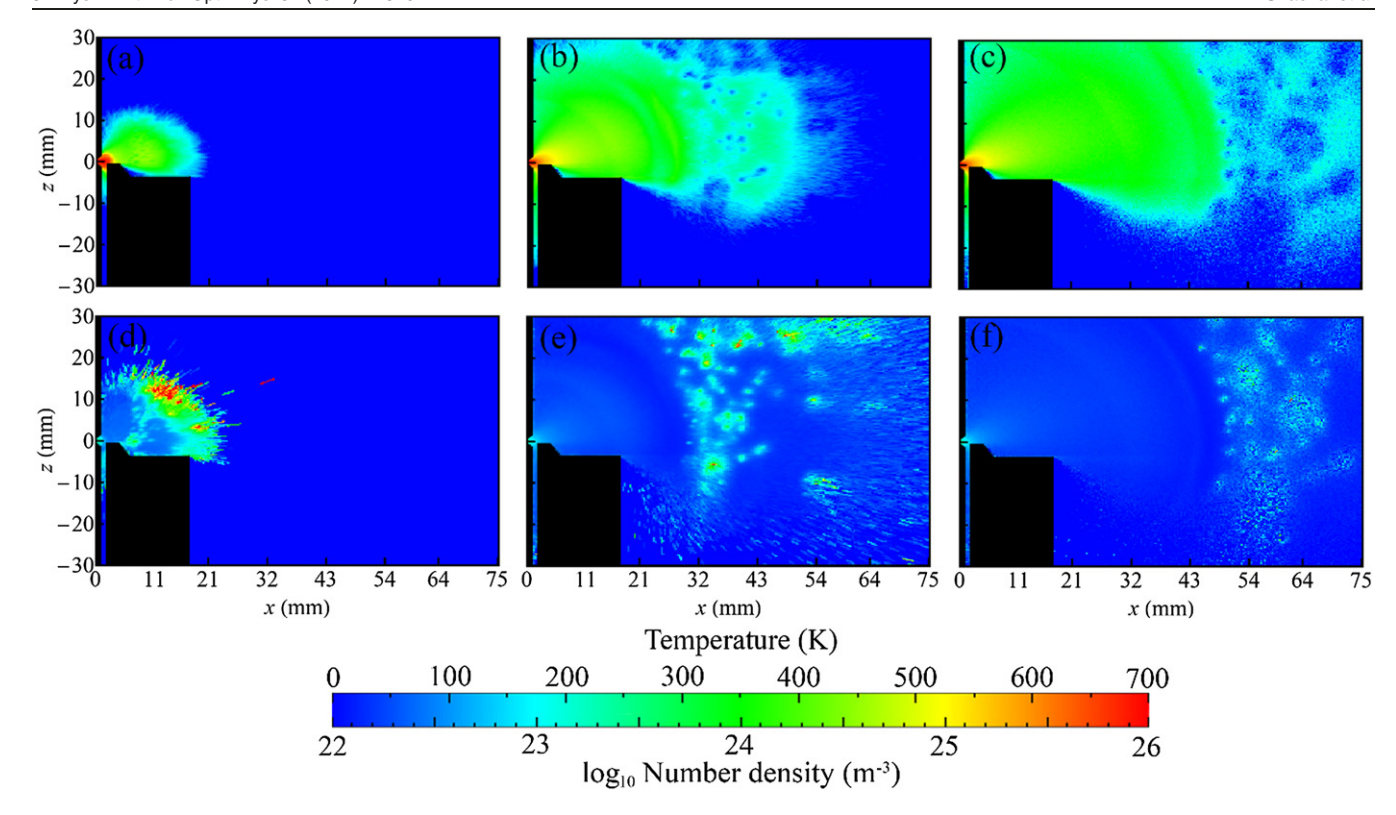


Figure 7. Snapshots of simulated number density (a)–(c) and temperature (d)–(f) of Ar with desorption of TRA molecules from the top of a sample bar, placed 0.6 mm below the center of the valve orifice. Snapshots taken at \sim 13 (a), (d), \sim 42 (b), (e), and \sim 65 μ s (c), (f) following valve opening.

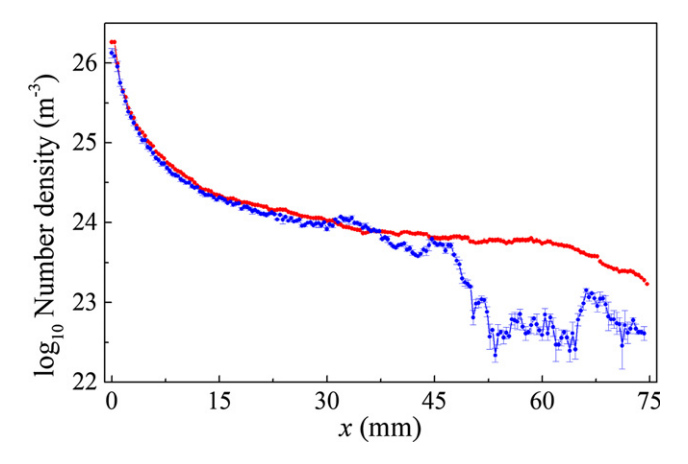


Figure 8. Average (blue) of three simulations of the on-axis Ar number density (including standard error bars), from the nozzle (0 mm) to the skimmer base (75 mm), at a time of \sim 65 μ s following gas entrance, as compared to the curve of the steady-state simulation, without desorption (red).

At this point, we should emphasize that ejection of large droplets or chunks of material in LD is possible [37]; however, our simulations considered only the related molecules and Ar atoms. Knochenmuss and Zhigilei [35] attribute the ejection of large droplets and chunks of material to photomechanical effects, driven by the relaxation of laser-induced stresses, being significant under conditions of stress confinement, at laser pulse durations shorter than the time needed for mechanical expansion of the absorbing volume. In the

experiments discussed here, we use ns laser pulses in the near-infrared of low fluence (0.4 J cm⁻²) for LD of samples embedded in graphite. Therefore, it seems that the conversion of the deposited laser energy to heat should be efficient, reducing the significant contribution of photomechanical effects. Moreover, 100 mJ cm⁻² or higher fluences are required to affect material ejection by ns laser pulses [71]. Hence, at our experimental conditions, a minimal effect is expected.

3.2. Source characterization

The intensity of the ionization signal of the MB produced by the LD source depends on both desorption and ionization delays requiring optimization of one before the other. Assisted by the DSMC simulation results, with the center of the Ar number density reaching the interaction point in the TOFMS at 290 μ s after valve opening (figure 4), optimization of the ionization laser pulse is possible. Hence, as a preliminary step, we probe the longitudinal (temporal) profile of the flow of the carrier gas (Ar), following its pre-mixing with toluene (C₆H₅CH₃), ionized by a 266 nm laser beam. Probing distinctive portions of the MB, by variation of the delay between the ionizing laser and the valve, results in different intensities of the toluene ionization signal. The temporal evolution shows that the maximum signal intensity occurs at a \sim 580 μ s, valve opening delay, comparable to that for a similar pulsed valve [5]. An extra \sim 300 μ s delay, related to the onset of the electrical signal and the gas pulse, is due to the coil electrical impedance and the mechanical inertia of the moving parts [72].

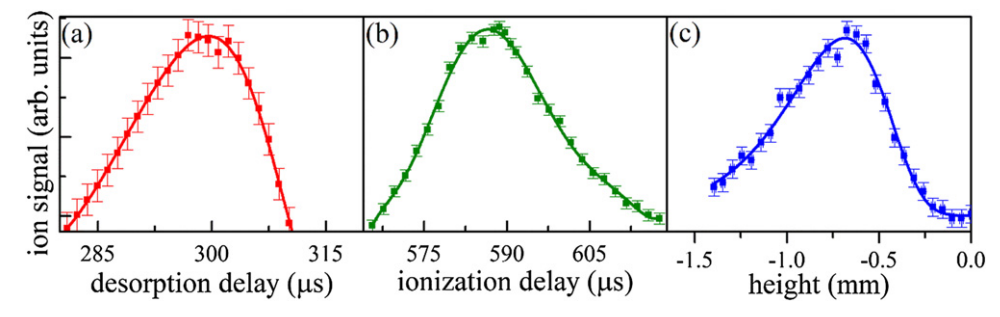


Figure 9. Measurements of resonance enhanced two-photon ionization signal (with standard error bars) of desorbed TRA at 34 919 cm⁻¹ as a function of the (a) desorption delay, (b) ionization delay, and (c) sample height relative to the orifice center.

For desorbed material, the optimum signal also depends on the desorption time. The delay is affected by two main factors: the interval required for the supersonic jet to form and propagate through the chamber reaching the sample and the desorbed plume formation. The desorption delay profile in figure 9(a) predominantly results from the vapor plume spatial shape.

After optimizing the delay for TRA desorption, optimization of the ionization delay is possible. We perform iterative optimization of these parameters, leading to the ionization profile for TRA as a function of the ionization laser delay in figure 9(b). An asymmetric shape ionization profile is obtained, reflecting a faster jet formation and a slower decay. The absolute delay values depend on many variables, such as chamber pressure, backing pressure, chamber length, and valve specifications.

Figure 9(c) shows the ionization signal as a function of the sample bar height (relative to the pulsed valve center). The profile shape is a result of three distinct effects: (1) the upward jet deflection caused by the sample bar, [5] leading to an optimal jet height that directs the densest and coldest MB portion into the skimmer; (2) signal loss due to substantial obstruction of the valve orifice for sample heights of -0.4 mm or more; and (3) reduction of the amount of entrained material, occurring with decreasing sample height, due to the spatial shape of the vapor plume. This behavior also agrees with the results of figures 5 and 6 that estimate the Ar density passing through the skimmer by positioning the sample bar at different heights and its translational temperature at the presence or absence of the sample bar. Both the simulation and the experimental results show that the sample bar strongly affects the supersonic expansion and hence the produced MB. Consequently, we had to compromise with its presence at a height that interferes less with the MB.

3.3. Mass and resonance enhanced two-photon ionization spectra of TRA

Figure 10(a) shows the MS of laser desorbed TRA at low ionization laser energy ($<1~\mu\text{J}$) at 34 919 cm⁻¹, the S₁ \leftarrow S₀ transition for the lowest energy conformer [43, 46, 52]. The spectrum shows only the parent ion signal at m/z = 160. Figure 9(b) shows the MS of TRA for more than two orders of magnitude higher laser energy (300 μ J),

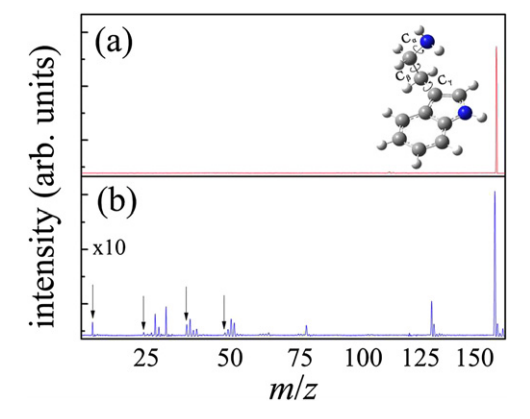


Figure 10. LD time of flight MS of TRA at the $S_1 \leftarrow S_0$ transition of the lowest energy conformer (34 919 cm $^{-1}$), using 0.4 mJ cm $^{-2}$ fluence for LD, argon at a 10 bar backing pressure, and ionization laser energy (a) <1 and (b) \sim 300 μ J. The inset in (a) shows the calculated structure, at the B3LYP/6-311++G(d,p) level of theory, of the most prominent conformer of TRA. The down-pointing arrows mark fragments of carbon and multiple carbons.

where in addition to the parent ion, several low-intensity fragments related to TRA appear. Also, the peak at m/z=12 and its multiplicities (marked by down-pointing arrows) are carbon and multiple carbons, resulting from TRA fragmentation and probably, to some extent, from the graphite matrix used for sample preparation. These findings imply that the dominant component in the MB is TRA, but we can not completely rule out material and matrix ejection. However, the formation of a uniform stripe in the sample by LD (not shown) and the low ionization energy use that generates a consistent parent ion signal, produced with low ionization laser fluence, point to the possibility to probe the LD TRA solely.

Figure 11 shows the resulting one-color R2PI spectrum of TRA. This spectrum includes conformational features of TRA in the region of the origins of the $S_1 \leftarrow S_0$ electronic transitions. These features match those observed in previously reported spectra, produced by thermal vaporization [43, 44, 46, 52]. Some differences in band intensities occur, probably due to signal saturation and slight differences in rotational temperatures and laser bandwidths. The TRA band intensities match well those we previously observed with thermal vaporization and under otherwise comparable experimental conditions [52], suggesting similar cooling of the entrained

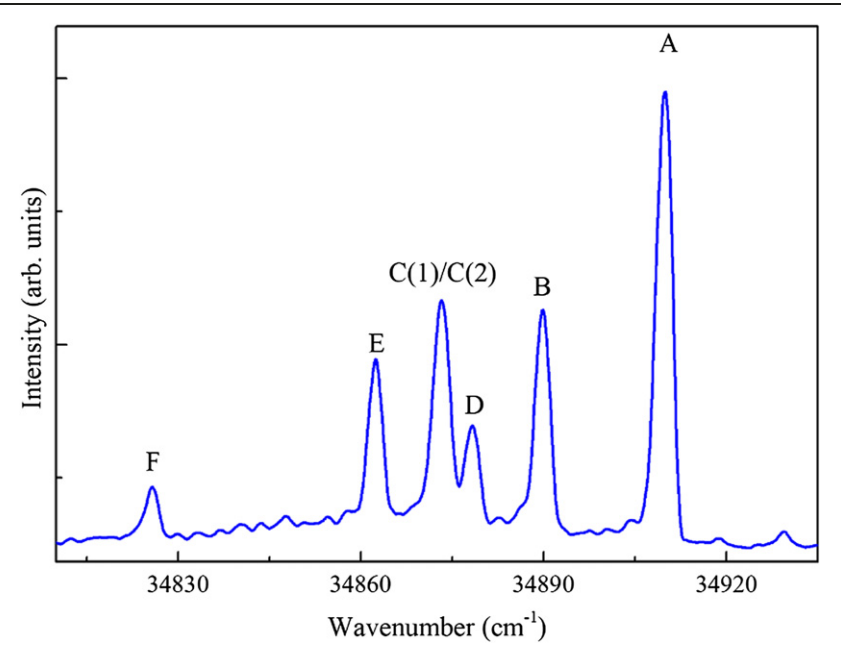


Figure 11. Resonance-enhanced two-photon ionization spectrum of jet cooled TRA (m/z = 160), obtained by LD at a 0.4 mJ cm⁻² fluence and carried by argon at a backing pressure of 10 bar to the interaction region. The jet-cooled molecules were excited in the $S_1 \leftarrow S_0$ band origin region and monitored at the ion peak. The observed transitions are related to different conformers, labeled according to references [43, 46].

molecules. Based on the achieved matching between the measured R2PI and simulated spectra of TRA molecules [52], the rotational temperature is of 15 K under the expansion conditions of our experiment. This temperature is comparable to the 17 K translational temperature of Ar that we deduced from the simulation results, following passage of the MB through the skimmer, figure 6. The labels A, B, C1/C2, D, E, and F for the distinct features, are adopted from previous studies and are assigned to the origins of seven conformers, consistent with the predicted lowest-energy conformers [46, 52].

Briefly, the observed conformers are distinguished by the torsional angles about the C_{α} - C_{β} and the C-N bonds in the ethylamino side chain (see the inset of figure 10(a)). The C_{α} - C_{β} torsion leads to different positions of the amine group relative to the indole, labeled A-F. Specifically, the resulting conformers include structures with an extended or folded side chain, i.e. anti or gauche conformers. In the latter, the amine group direction is toward the pyrrole or phenyl side of indole. The most prominent feature in the R2PI spectrum belongs to the predominant gauche conformer, Gpy(out), inset of figure 10(a), where the amino group is in the gauche conformation near the pyrrole side and pointing away from the indole π cloud. Stabilization of this configuration occurs by a weak H-bond formed between the amino hydrogen and the pyrrole π cloud, but probably additional interactions might also be of importance.

4. Summary

We demonstrate a compact and cost-effective LD source for MB generation. DSMC simulation results allow the analysis

of the gas flow, the cooling characteristics of the desorbed compound and assist in optimizing the timing required for spectroscopic measurements with this source.

The selected operating conditions for source and system permit the first spectral measurements, including MS and R2PI spectra of LD TRA. The R2PI spectral signature consists of the same conformational features as those obtained for heated samples, showing evidence for the presence of seven conformers in the MB, and demonstrating efficient cooling conditions. The coupling of this source to other systems and its use in future studies may bring new spectral measurements within reach for illuminating the structure and dynamics of biomolecules.

Acknowledgments

We would like to acknowledge the financial support of this research by the United States—Israel Binational Science Foundation (BSF) under Grant 2014370 and the Israel Science Foundation (ISF) founded by the Israel Academy of Sciences and Humanities, Grant No. 519/15. This work was also supported by the National Science Foundation (NSF) under CHE-1800283.

Data availability statement

The data generated and/or analysed during the current study are not publicly available for legal/ethical reasons but are available from the corresponding author on reasonable request.

ORCID iDs

Afik Shachar https://orcid.org/0000-0002-1232-0816

Mattanjah S de Vries https://orcid.org/0000-0001-5007-8074

Ilana Bar (b) https://orcid.org/0000-0002-4032-1904

References

- Herschbach D R 1962 Reactive collisions in crossed molecular beams *Discuss. Faraday Soc.* 33 149–61
- [2] Tembreull R and Lubman D M 1987 Resonant two-photon ionization in biomolecules using laser desorption in supersonic beam-mass spectrometry Appl. Spectrosc. 41 431–6
- [3] Rizzo T R, Park Y D and Levy D H 1985 A molecular beam of tryptophan J. Am. Chem. Soc. 107 277–8
- [4] Boesl U, Grotemeyer J, Walter K and Schlag E W 1987 Resonance ionization and time-of-flight mass spectrometry, high resolution, involatile molecules *Resonance Ionization Spectroscopy* vol 369, ed G S Hurst and C G Morgan (Bristol: Institute of Physics Publishing) pp 223–8
- [5] Arrowsmith P, de Vries M S, Hunziker H E and Wendt H R 1988 Pulsed laser desorption near a jet orifice: concentration profiles of entrained perylene vapor Appl. Phys. B 46 165–73
- [6] Levis R J 1994 Laser desorption and ejection of biomolecules from the condensed phase into the gas phase Annu. Rev. Phys. Chem. 45 483–518
- [7] Schwing K and Gerhards M 2016 Investigations on isolated peptides by combined IR/UV spectroscopy in a molecular beam-structure, aggregation, solvation and molecular recognition *Int. Rev. Phys. Chem.* 35 569–677
- [8] Rijs A M and Oomens J 2015 IR spectroscopic techniques to study isolated biomolecules in Gas-Phase IR Spectroscopy and Structure of Biological Molecules ed ed A M Rijs and J Oomens (Berlin: Springer) chapter 1 pp 1–42
- [9] Gloaguen E and Mons M 2015 Isolated neutral peptides in Gas-Phase IR Spectroscopy and Structure of Biological Molecules ed ed A M Rijs and J Oomens (Berlin: Springer) pp 225–70
- [10] Kleinermanns K, Nachtigalloa D and de Vries MS 2013 Excited state dynamics of DNA bases Int. Rev. Phys. Chem. 32 308–42
- [11] Simons J P 2009 Good vibrations: probing biomolecular structure and interactions through spectroscopy in the gas phase Mol. Phys. 107 2435–58
- [12] de Vries M S and Hobza P 2007 Gas-phase spectroscopy of biomolecular building blocks *Annu. Rev. Phys. Chem.* 58 585-612
- [13] Abo-Riziq A, Crews B O, Callahan M P, Grace L and de Vries M S 2006 Angew. Chem., Int. Ed. 45 5166–9
- [14] Nir E, Kleinermanns K and de Vries M S 2000 Pairing of isolated nucleic-acid bases in the absence of the DNA backbone Nature 408 949–51
- [15] Nir E, Imhof P, Kleinermanns K and de Vries M S 2000 REMPI spectroscopy of laser desorbed guanosines J. Am. Chem. Soc. 122 8091–2
- [16] Anex D S, de Vries M S, Knebelkamp A, Bargon J, Russell Wendt H and Hunziker H E 1994 Resonanceenhanced two-photon ionization time-of-flight spectroscopy of cold perfluorinated polyethers and their external and internal van der Waals dimers *Int. J. Mass Spectrom.* 131 319–34
- [17] Cromwell E F, Reihs K, de Vries M S, WendtGhaderi H R, Hunziker H E and Hunziker H E 1993 Transition-metal cationization of laser desorbed perfluorinated polyethers with FTICR mass spectrometry J. Phys. Chem. 97 4720–8
- [18] Saigusa H, Tomioka A, Katayama T and Iwase E 2006 A matrixfree laser desorption method for production of nucleobase clusters and their hydrates Chem. Phys. Lett. 418 119–25

- [19] Tembreull R and Lubman D M 1986 Pulsed laser desorption with resonant two-photon ionization detection in supersonic beam mass spectrometry *Anal. Chem.* 58 1299–303
- [20] Meijer G, de Vries M S, WendtHunziker H R and Wendt H R 1990 Laser desorption jet-cooling of organic molecules Appl. Phys. B 51 395–403
- [21] Karas M, Bachmann D, Bahr U and Hillenkamp F 1987 Matrixassisted ultraviolet laser desorption of non-volatile compounds Int. J. Mass Spectrom. Ion Process. 78 53–68
- [22] Tanaka K, Waki H, Ido Y, Akita S, Yoshida Y, Yoshida T and Matsuo T 1988 Protein and polymer analyses up tom/z 100 000 by laser ionization time-of-flight mass spectrometry Rapid Commun. Mass Spectrom. 2 151–3
- [23] El-Aneed A, Cohen A and Banoub J 2009 Mass spectrometry, review of the basics: electrospray, MALDI, and commonly used mass analyzers Appl. Spectrosc. Rev. 44 210–30
- [24] Mandal A, Singha M, Addy P S and Basak A 2019 Laser desorption ionization mass spectrometry: recent progress in matrix-free and label-assisted techniques *Mass Spec. Rev.* 38 3–21
- [25] Hall R B 1987 Pulsed-laser-induced desorption studies of the kinetics of surface reactions J. Phys. Chem. 91 1007–15
- [26] Li Y, McIver R T and Hemminger J C 1990 Experimental determination of thermal and nonthermal mechanisms for laser desorption from thin metal films J. Chem. Phys. 93 4719–23
- [27] Zenobi R, Hahn J H and Zare R N 1988 Surface temperature measurement of dielectric materials heated by pulsed laser radiation *Chem. Phys. Lett.* 150 361–5
- [28] Philippoz J-M, Zenobi R and Zare R N 1989 Pulsed heating of surfaces: comparison between numerical simulation, analytical models, and experiments *Chem. Phys. Lett.* 158 12–7
- [29] Voumard P, Zenobi R and Zhan Q 1995 Spectroscopic probe for energy transfer during laser desorption from surfaces *J. Phys. Chem.* 99 11722–7
- [30] Piuzzi F, Dimicoli I, Mons M, Tardivel B and Zhao Q 20002000 A simple laser vaporization source for thermally fragile molecules coupled to a supersonic expansion: application to the spectroscopy of tryptophan Chem. Phys. Lett. 320 282–8
- [31] Taherkhani M, Riese M, BenYezzar M and Muller-Dethlefs K 2010 A novel experimental system of high stability and lifetime for the laser-desorption of biomolecules *Rev. Sci. Instrum.* 81 063101
- [32] Ishiuchi S-i., Yamada K, Oba H, Wako H and Fujii M 2016 Gas phase ultraviolet and infrared spectroscopy on a partial peptide of β 2-adrenoceptor SIVSF-NH2 by a laser desorption supersonic jet technique *Phys. Chem. Chem. Phys.* 18 23277–84
- [33] Teschmit N, Długołecki K, Gusa D, Rubinsky I, Horke D A and Küpper J 2017 Characterizing and optimizing a laser-desorption molecular beam source J. Chem. Phys. 147 144204
- [34] Karim E T, Wu C and Zhigilei L V 2014 Molecular dynamics simulations of laser-materials interactions: general and material-specific mechanisms of material removal and generation of crystal defects Fundamentals of Laser-Assisted Micro- and Nanotechnologies (Springer Series in Materials Science) vol 195, ed V Veiko and V Konov (Berlin: Springer)
- [35] Knochenmuss R and Zhigilei L V 2005 Molecular dynamics model of ultraviolet matrix-assisted laser desorption/ionization including ionization processes J. Phys. Chem B 109 22947–57
- [36] Leveugle E, Ivanov D S and Zhigilei L V 2004 Photomechanical spallation of molecular and metal targets: molecular dynamics study Appl. Phys. A 79 1643
- [37] Zhigilei L V, Leveugle E, Garrison B J, Yingling Y G and Zeifman M I 2003 Computer simulations of laser ablation of molecular substrates Chem. Rev. 103 321–48

- [38] Zhigilei L V, Kodali P B S and Garrison B J 1997 Molecular dynamics model for laser ablation and desorption of organic solids J. Phys. Chem B 101 2028–37
- [39] Morozov A A 2013 Interpretation of time-of-flight distributions for neutral particles under pulsed laser evaporation using direct Monte Carlo simulation J. Chem. Phys. 139 234706
- [40] Itina T E, Marine W and Autric M 1998 Monte Carlo simulation of pulsed laser ablation into an ambient gas *Comput. Mater.* Sci. 10 144–7
- [41] Zeifman M I, Garrison B J and Zhigilei L V 2002 Combined molecular dynamics-direct simulation Monte Carlo computational study of laser ablation plume evolution *J. Appl. Phys.* 92 2181–93
- [42] Bird G A 1994 Molecular Gas Dynamics and the Direct Simulation of Gas Flows (Oxford: Clarendon)
- [43] Park Y D, Rizzo T R, Peteanu L A and Levy D H 1986 Electronic spectroscopy of tryptophan analogs in supersonic jets: 3-indole acetic acid, 3-indole propionic acid, tryptamine, and N-acetyl tryptophan ethyl ester J. Chem. Phys. 84 6539–49
- [44] Philips L A and Levy D H 1986 Determination of the transition moment and the geometry of tryptamine by rotationally resolved electronic spectroscopy *J. Phys. Chem.* **90** 4921–3
- [45] Philips L A and Levy D H 1988 Rotationally resolved electronic spectroscopy of tryptamine conformers in a supersonic jet *J. Chem. Phys.* **89** 85–90
- [46] Carney J R and Zwier T S 2000 The infrared and ultraviolet spectra of individual conformational isomers of biomolecules: tryptamine J. Phys. Chem A 104 8677–88
- [47] Schmitt M, Feng K, Böhm M and Kleinermanns K 2006 Low frequency backbone vibrations of individual conformational isomers: Tryptamine J. Chem. Phys. 125 144303
- [48] Nguyen T V and Pratt D W 2006 Permanent electric dipole moments of four tryptamine conformers in the gas phase: a new diagnostic of structure and dynamics J. Chem. Phys. 124 054317
- [49] Gu Q and Knee J L 2012 Zero kinetic energy photoelectron spectroscopy of tryptamine and the dissociation pathway of the singly hydrated cation cluster J. Chem. Phys. 137 104312
- [50] Sakota K, Kouno Y, Harada S, Miyazaki M, Fujii M and Sekiya H 2012 IR spectroscopy of monohydrated tryptamine cation: rearrangement of the intermolecular hydrogen bond induced by photoionization *J. Chem. Phys.* 137 224311
- [51] Mayorkas N, Izbitski S, Bernat A and Bar I 2012 Simultaneous ionization-detected stimulated Raman and visible-visible-ultraviolet hole-burning spectra of two tryptamine conformers J. Phys. Chem. Lett. 3 603–7
- [52] Mayorkas N, Bernat A, Izbitski S and Bar I 2013 Vibrational and vibronic spectra of tryptamine conformers J. Chem. Phys. 138 124312
- [53] Schmitt M, Spiering F, Zhaunerchyk V, Jongma R T, Jaeqx S, Rijs A M and van der Zande W J 2016 Far-infrared spectra of the tryptamine A conformer by IR–UV ion gain spectroscopy *Phys. Chem. Chem. Phys.* 18 32116–24
- [54] Luria K, Christen W and Even U 2011 Generation and propagation of intense supersonic beams J. Phys. Chem A 115 7362-7
- [55] Irimia D, Dobrikov D, Kortekaas R, Voet H, van den Ende D A, Groen W A and Janssen M H M 2009 A short pulse

- (7 μs FWHM) and high repetition rate (dc-5 kHz) cantilever piezovalve for pulsed atomic and molecular beams *Rev. Sci. Instrum.* **80** 113303
- [56] Gentry W R and Giese C F 1978 Ten-microsecond pulsed molecular beam source and a fast ionization detector *Rev. Sci. Instrum.* 49 595–600
- [57] Yan B, Claus P F H, van Oorschot B G M, Gerritsen L, Eppink A T J B, van de Meerakker S Y T and Parker D H 2013 A new high intensity and short-pulse molecular beam valve *Rev. Sci. Instrum.* 84 023102
- [58] Even U 2015 The Even-Lavie valve as a source for high intensity supersonic beam *EPJ Tech. Instrum.* **2** 1–22
- [59] Wall T E 2016 Preparation of cold molecules for highprecision measurements J. Phys. B: At. Mol. Opt. Phys. 49 243001
- [60] Sheppard R G, Morgan D, Mathes D M and Bray D J (ed) 2002 Properties and Characteristics of Graphite (Decatur, TX: Poco Graphite, Inc.)
- [61] Epshtein M, Portnov A, Kupfer R, Rosenwaks S and Bar I 2013 Enhanced sensitivity in H photofragment detection by two-color reduced-Doppler ion imaging J. Chem. Phys. 139 184201
- [62] Shachar A, Mayorkas N, Sachs H and Bar I 2017 The conformational landscape of 2-(4-fluoro-phenyl)-ethylamine: consequences of fluorine substitution at the para position *Phys. Chem. Chem. Phys.* 19 510–22
- [63] Shachar A, Mayorkas N and Bar I 2017 Structural features of monohydrated 2-(4-fluorophenyl)ethylamine: a combined spectroscopic and computational study *Phys. Chem. Chem. Phys.* 19 23999–4008
- [64] Shu C, Mao X H and Chew Y T 2005 Particle number per cell and scaling factor effect on accuracy of DSMC simulation of micro flows Int. J. Numer. Methods Heat Fluid Flow 15 827–41
- [65] Gallis M A, Torczynski J R, Plimpton S J, Rader D J and Koehler T 2014 Direct simulation Monte Carlo: the quest for speed AIP Conf. Proc. 1628 27–36
- [66] Borgnakke C and Larsen P S 1975 Statistical collision model for Monte Carlo simulation of polyatomic gas mixture J. Comput. Phys. 18 405–20
- [67] Becke A D 1988 Density-functional exchange-energy approximation with correct asymptotic behavior *Phys. Rev.* A 38 3098–100
- [68] Lee C, Yang W and Parr R G 1988 Development of the Colle-Salvetti correlation-energy formula into a functional of the electron density *Phys. Rev.* B 37 785–9
- [69] Bird G A 2005 The DS2V/3V Program suite for DSMC calculations AIP Conf. Proc. 762 541–6 DS2V, version 4.5.06 http://gab.com.au/page4.html
- [70] Scoles G (ed) 1988 Atomic and Molecular Beam Methods (Oxford: Oxford University Press)
- [71] Georgiou S and Koubenakis A 2003 Laser-induced material ejection from model molecular solids and liquids: mechanisms, implications, and applications *Chem. Rev.* 103 349–94
- [72] Abad L, Bermejo D, Herrero V J, Santos J and Tanarro I 1995 Performance of a solenoid-driven pulsed molecular-beam source Rev. Sci. Instrum. 66 3826–32